Article

Direct Observation of Short Large-Amplitude Magnetic Field Structures from Formation to Destruction

Shi-Chen Bai [1,2,*] , Quanqi Shi [2,*] , Ruilong Guo [2] , Alexander W. Degeling [2] , Hui Zhang [2], Anmin Tian [2] and Yude Bu [1]

1   School of Mathematics and Statistics, Shandong University, Weihai 264209, China; buyude@sdu.edu.cn
2   Shandong Provincial Key Laboratory of Optical Astronomy and Solar-Terrestrial Environment, Institute of Space Sciences, Shandong University, Weihai 264209, China; grl@sdu.edu.cn (R.G.); degeling@sdu.edu.cn (A.W.D.); h.zhang@sdu.edu.cn (H.Z.); tamin@sdu.edu.cn (A.T.)
*   Correspondence: bsc@sdu.edu.cn (S.-C.B.); sqq@sdu.edu.cn (Q.S.)

Abstract: Short large-amplitude magnetic field structures (SLAMSs) are often seen upstream of quasi-parallel shocks. They play vital roles near the quasi-parallel shock, such as decelerating solar wind ions and contributing to the dissipation and reformation of the shock. The formation process of these structures has attracted great attention and has long been realized in simulation. However, their formation mechanism is still full of mysteries. Here, using magnetospheric multiscale mission (MMS) observation, we provide direct observations of the SLAMS formation and destruction processes. SLAMS growth is powered by solar wind ions and shock-reflected ions through the ion-ion non-resonant mode. Reconnection occurs between and inside SLAMSs during their growth; however, these cumulative changes in magnetic field topology and the dissipation of the magnetic field energy contribute to the destruction of the SLAMS. These observations shed new light on the dissipation and reformation of the shock both in space physics and astrophysics.

Keywords: bow shock; short large-amplitude magnetic field structures ion-ion two stream instability; magnetic reconnection

1. Introduction

Collisionless shocks are commonly observed in space physics [1–3]. When the plasma's kinetic energy exceeds the shock's dissipation limit, a portion is reflected upstream, exciting different ion-ion two-stream instabilities [4]. This interaction generates ultra-low frequency (ULF) waves and leads to the formation of different kinds of non-linear compressional magnetic structures [5–8].

SLAMSs stand out among these structures and play crucial roles near the shock [9–11]. They exhibit substantial magnetic field enhancements ($\delta B/B_0 > 2$ [12], where δB is the magnetic field enhancement and B_0 is the background magnetic field). Similar to the quasi-perpendicular shocks, SLAMSs decelerate, thermalize, and reflect solar wind ions in the foreshock region [13–15]. In addition, SLAMSs contribute to electron acceleration and generation of whistler-mode waves [16,17], shock dissipation and reformation [18,19], magnetic reconnection [20–27], and energy cascades within the turbulence at the quasi-parallel shock [28], leading to the downstream generation of a magnetosheath high-speed jet [29–31].

Based on theoretical and numerical studies of the evolution of SLAMSs [4,32], SLAMSs can be generated by different modes of ion-ion two-stream instabilities: the ion-ion right-hand non-resonant mode [33,34] and the ion-ion right-hand and left-hand resonant mode [35,36]. The distinctions among these modes lie in the wave period, polarization, and propagation direction in the plasma rest frame. SLAMSs undergo significant steepening near the bow shock [37,38]. Their convection speed (relative to the bow shock) decreases

with increasing amplitude and decreasing distance to the bow shock [12,39]. SLAMS formation has been long realized in simulation [6,40,41]. Research using hybrid simulations has found that SLAMSs can be created by electromagnetic ion/ion beam instabilities [7,8,34]. Meanwhile, particle-in-cell (PIC) simulations suggest that shocklets and SLAMSs can arise from a nonlinear interaction between gradients in ion densities and the ULF wave field [40,41]. However, cluster observation reveals fundamentally different properties between SLAMSs and ULF-related structures [10,11]. By comparing the analytical approximations [4,34] with wind observation, Wilson et al. [15] argue that the ion-ion instability, while reaching saturation, is insufficient to account for the strong magnetic fields observed in SLAMSs. Recent findings from the magnetospheric multiscale (MMS) mission shed light on this phenomenon. Chen et al. [42] suggests that the anomalous resonance between solar wind ions and ULF waves could play a pivotal role in the magnetic amplification from quasi-sinusoidal waves to SLAMSs.

The formation mechanism of SLAMSs is still full of mysteries. However, direct in-situ satellite observation following the rise and fall of individual SLAMSs has not been reported in the literature. In this paper, using unprecedented MMS observation [43–47] when MMS 1–4 are positioned in a single line, we provide direct observations of the rise and fall of SLAMSs.

2. Data

The data used in this study is obtained from the MMS1–4 satellite burst-mode observation. The solar wind data is obtained from the OMNI data set. Since the ion moment data from MMS in the solar wind might not be so reliable, the drift bi-Maxwellian distribution is used to fit the observed ion distribution using the equation shown below.

$$f_{ion}\left(V_{\parallel},V_{\perp}\right) = \frac{n_{ion}}{\pi^{3/2}V_{th\parallel}V_{th\perp}^2}exp\left(-\frac{\left(V_{\parallel}-V_{drift\parallel}\right)^2}{V_{th\parallel}^2}-\frac{\left(V_{\perp}-V_{drift\perp}\right)^2}{V_{th\perp}^2}\right) \quad (1)$$

where V_{th} and V_{drift} denote the ion thermal speed and ion drift speed, respectively. $\parallel$ and $\perp$ denote the velocity parallel and perpendicular to the local magnetic field.

3. Results

Figure 1 shows four satellite MMS burst-mode observations on 30 January 2019, from 14:47:43.5 to 14:47:55 UT. The MMS constellation is positioned near the quasi-parallel bow shock (Figure 1i, $\theta_{BN} = 20°$ and $M_A = 14.8$). θ_{BN} represents the angle between the interplanetary magnetic field vector (OMNI data set: [1.81, 1.16, 0.77] nT in GSM) and the bow shock normal (determined via a model [48]). M_A is the solar wind Alfvén Mach number. The four MMS spacecraft align in a line. After MMS3 encountered SLAMSs first, MMS4 followed, then MMS1, and finally MMS2. Figure 1 shows their encounters from top to bottom in this order. To display the SLAMSs evolution clearly, the four satellite observations are time-shifted with respect to the MMS3 time series. The lag time ($\Delta t = 2.1$ s) between MMS3 and MMS4 is determined based on the correlation coefficient (cc = 0.88 when $\Delta t = 2.1$ s) between the profile of the magnetic field from MMS3 and time shifted MMS4 observation. For MMS1 and MMS2, the lag time is determined by the distance to MMS3 and the propagation velocity of the SLAMSs. The propagation velocity of these SLAMSs in GSM coordinates is obtained [−168.0, 29.8, −48.5] km/s using the lag time and satellite separation between MMS3 and MMS4.
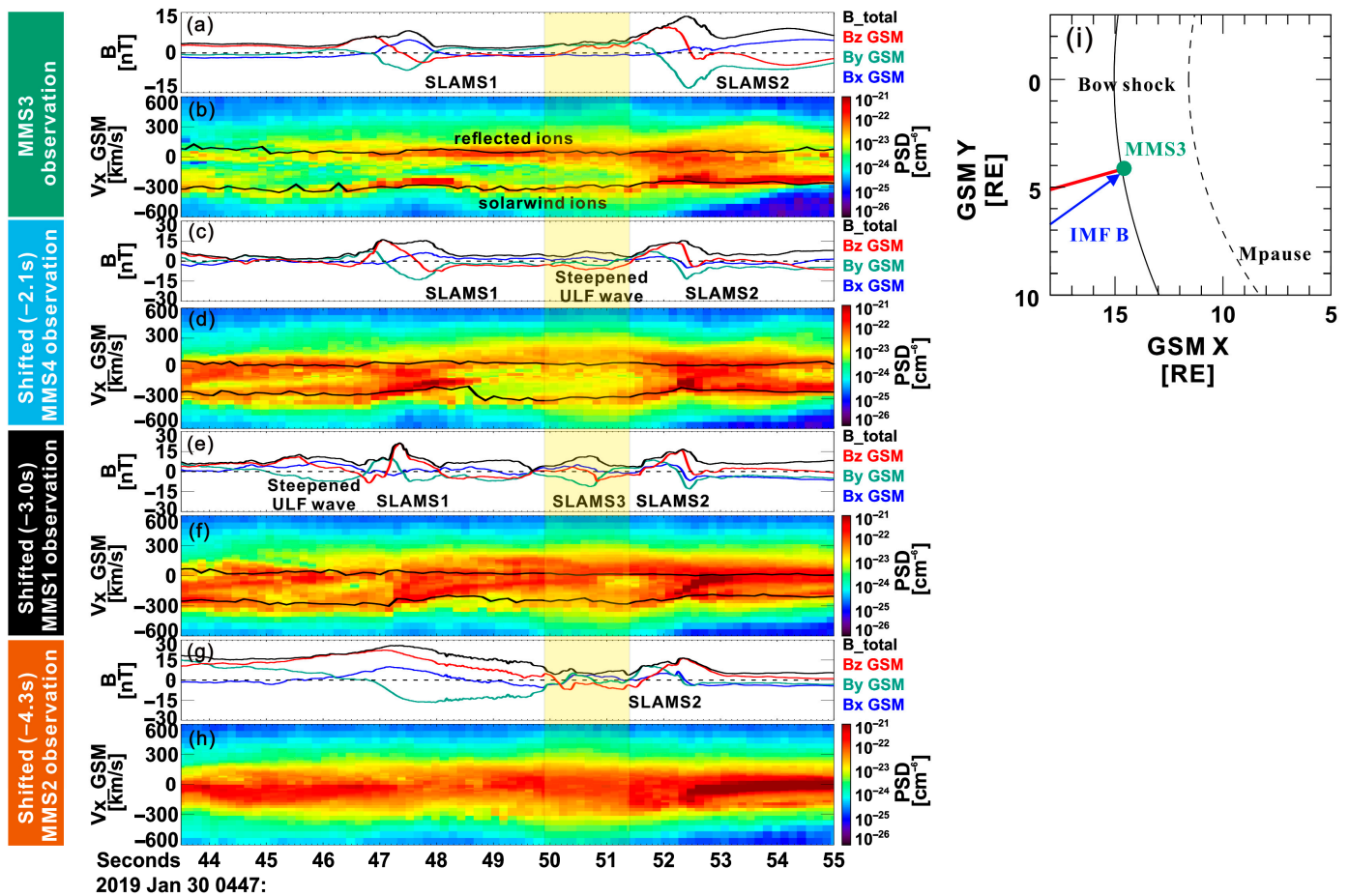
Figure 1. Magnetic field and reduced ion distribution as a function of Vx_GSM observed by (**a**,**b**) MMS3 (green bar on the left), (**c**,**d**) MMS4 (cyan bar on the left), (**e**,**f**), MMS1 (black bar on the left), and (**g**,**h**) MMS2 (orange bar on the left). The bulk velocity of the solar wind and reflected ions (black lines) are overlaid on the reduced ion distribution in (**b**,**d**,**f**). X/Y/Z component in GSM coordinate system is represented by blue/green/red curve. Burst-mode observation of MMS1, MMS2, and MMS4 are time-shifted to MMS3. The time interval of the SLAMSs evolution is highlighted by yellow shaded region. (**i**) The position of MMS3 (green dots), the interplanetary magnetic field (blue arrow), the normal direction of the bow shock (red line), bow shock (solid curve), and magnetopause (dashed line) obtained from the models [48] are shown in the GSM X-Y plane.

Figure 1b shows that MMS3 detects solar wind ion beams and the ion beams reflected by the bow shock or SLAMSs. In each case, their bulk velocity Vx is overlaid on the reduced ion distribution in the plot. Later observations by MMS4 and MMS1 (Figure 1d,f), show that both populations are thermalized presumably due to the ULF waves generated by the ion-ion two-stream instability, eventually merging into one population observed by MMS2 (Figure 1h). Simultaneously, SLAMS 1 (14:47:46.5 to 14:47:49 UT) and SLAMS 2 (14:47:51.5 to 14:47:53 UT) experience intense steepening based on the comparison of MMS3 and MMS1 observation, identified by enhanced magnetic fields (SLAMS 1: $\delta B/B_0 = 3.69$, $B_0 = 3.91$ nT; SLAMS 2: $\delta B/B_0 = 2.90$, $B_0 = 5.25$ nT) and solar wind ion deceleration (Figure 1d, f, at 14:47:47.4 UT for SLAMS 1 and 14:47:51.4 UT for SLAMS 2).

Between these two SLAMSs, the rise and fall of an additional SLAMS, (labelled SLAMS 3, 14:47:49.9 to 14:47:51.4 UT, highlighted in the yellow shaded region) is observed by the MMS constellation, starting as the leading edge of SLAMS 2 in MMS3, evolving into a steepened ULF wave ($\delta B/B_0 = 1.79$, $B_0 = 3.91$ nT) observed by MMS4 after approximately two seconds, becoming a SLAMS ($\delta B/B_0 = 2.81$, $B_0 = 3.91$ nT) observed by MMS1 after three seconds, and eventually breaking up rapidly as observed by MMS2.

Figure 2 shows the wavelet analysis of the magnetic field observed by four MMS satellites during the time periods of SLAMS 3 and SLAMS 2 (identified by the enhanced magnetic field and density in Figure 2). The wavelet analysis shows that the wave frequency with maximum amplitude f_{max} (f_{max} = 0.65 Hz = 2.83 f_{ci} black dashed lines in Figure 2, ion gyro-frequency f_{ci} = 0.23 Hz) falls within the expected ULF wave range generated by the non-resonant mode. In the spacecraft reference frame, the ULF wave polarization, analyzed through the hodograms of the magnetic field in the L-M plane (shown in Figure 2j–l), consistently exhibits right-hand circular polarization during the SLAMS 3 evolution. The L-M-N coordinates of the SLAMSs are determined by the minimum variance analysis of the magnetic field [49,50]. During the steepening, ULF waves with frequencies several times the f_{max} are generated ($f \sim 1.4$, 2.1 Hz) and superimposed on the original ULF wave (Figure 2 e,g within SLAMS 3 and SLAMS 2). These waves, having similar amplitudes and phase velocities to the original ULF waves, are harmonic sidebands. They, in turn, generate their own harmonic sidebands during the steepening process [28,51]. Subsequently, SLAMS 3 forms due to the steepening of these ULF waves. During the MMS2 observation, although strong ULF waves near the f_{max} persist (Figure 2i), the harmonic sidebands between f_{max} and lower-hybrid frequencies (black and white dashed lines in Figure 2) are weaker (Figure 2f) while the wave below f_{max} becomes stronger. These observational features are consistent with the evolution of SLAMSs generated using the ion-ion non-resonant mode in simulations [34]. The SLAMSs generated through the ion-ion non-resonant mode are subject to a parameter decay and tend to form a state of condensate where the turbulence becomes nearly monochromatic [34].
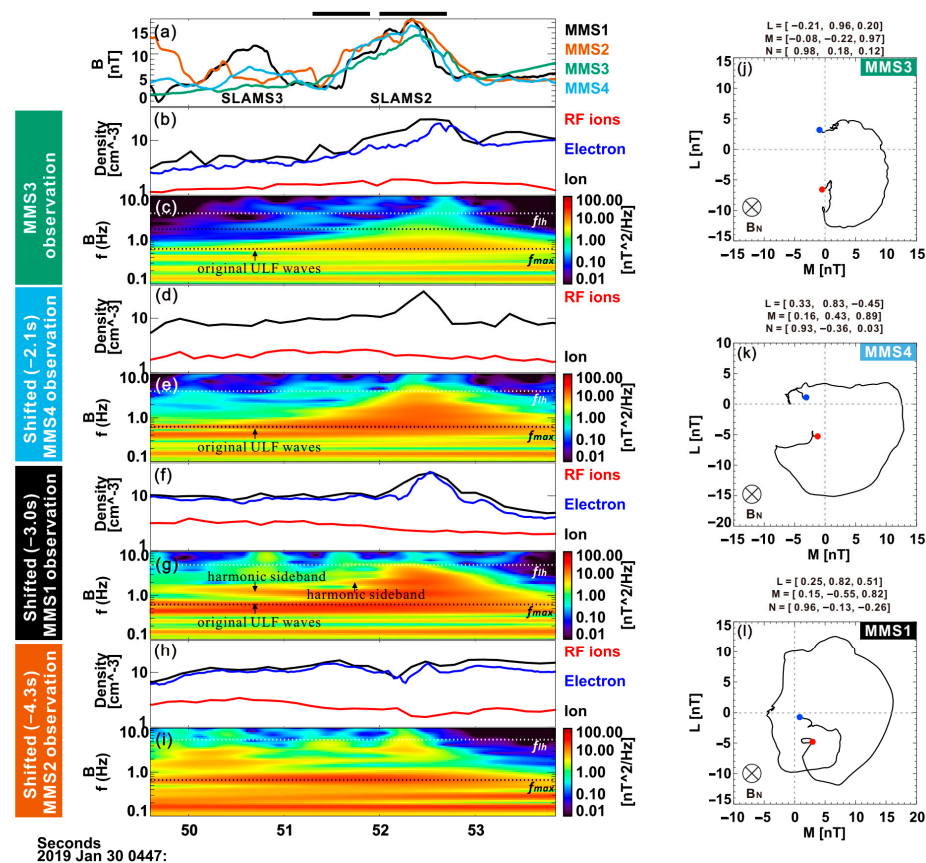

Figure 2. (**a**) The magnitude of magnetic field observed by MMS1 (black curve), MMS2 (orange curve), MMS3 (green curve), and MMS4 (cyan curve); plasma density (red/black/blue curves for reflected ion/ion/electron, electron data of MMS4 are not available) and wavelet power spectra of

the magnetic fields observed by (**b**,**c**) MMS3, (**d**,**e**) MMS4, (**f**,**g**), MMS1, and (**h**,**i**) MMS2. Burst-mode observation of MMS1, MMS2, and MMS4 are time-shifted to MMS3. The horizontal black and white dashed lines in wavelet power spectra indicate the f_{max} and the lower-hybrid frequency f_{lh}. The black bars on the top of (**a**) indicate the interval of magnetic reconnection. The hodogram of the magnetic field in the L-M plane observed by (**j**) MMS3, (**k**) MMS4, and (**l**) MMS1. The start and end points in (**j**,**k**) are marked by blue and red dots, respectively. The MMS3/4/1/2 observation are marked by green/cyan/black/orange bars in the left and (**j**,**k**).

In addition, key parameters determining the modes of the ion-ion two-stream instability are the density ratio and relative drift between the solar wind and reflected ions. The velocity and density of the two ion populations (n_{rf}/n_{sw} = 0.31 and ΔV = 339.53 km/s~8.0 $V_{Alfvén}$ from MMS observation, n_{rf}/n_{sw} = 0.28 and ΔV = 232.59 km/s~5.5 $V_{Alfvén}$ from bi-Maxwellian fitting, $V_{Alfvén}$ = 42.41 km/s) reveal favorable conditions for the excitation of the ion-ion right-hand non-resonant mode (modest density ratio and high relative drift $\Delta V \gg V_A$, see details in Table 2 from [4]). The phase velocity of the ULF wave ($V_{ph\_x} = \omega/k_x - 280$ km/s) and the wave vector k ($kd_i = 0.36$, ion inertial length $d_i = 116.84$ km) are determined based on the band-pass filtered magnetic field B and electric field E (0.3~2 Hz) through linearized Faraday's law ($k \times E = \omega B$). The ω is determined based on the f_{max} in wavelet analysis Figure 2e. Therefore, the ULF wave propagates toward Earth in the solar wind reference frame ($V_{sw\_x} = -251 \sim -240$ km/s in the spacecraft reference frame based on drift bi-Maxwellian fitting and MMS observation). Therefore, the ULF wave is Earthward, propagating in the solar wind rest frame generated through the ion-ion non-resonant mode.

To confirm the generation mechanism, we also used the linear dispersion solver BO [52] to solve the dispersion relation. The input plasma parameters are obtained via drift bi-Maxwellian fitting of the ion distribution (as shown in Figure 3). We only used the fitting results of MMS3 observations during the SLAMS 3 interval (yellow shaded area in Figure 1), which is the only satellite that observed ULF waves in the linear state. The detail parameters can be found in Table 1. Corresponding to input plasma parameters, only the ion-ion non-resonant mode has a positive growth rate. The dispersion relation of the ion-ion non-resonant mode is presented in Figure 4, which is consistent with the MMS observation. We also compare the enhanced magnetic fields (δB/B0) with the saturation amplitude of the ion-ion non-resonant mode based on the analytical approximations [34] from $\delta B/B0 \sim (n\_rf/n\_sw)^(1/2) (V\_drift\_rf/V\_th\_SW)$ using the parameters in Table 1. The observed enhancement is lower than the saturation amplitude as shown in Table 1, indicating that the ion-ion non-resonant mode is sufficient to drive the formation of SLAMS 3 observed by MMS.

Numerical simulations in previous studies have shown that the ion-ion non-resonant mode can generate current sheets inside SLAMSs and trigger magnetic reconnection [20,21]. Here, reconnection processes are identified by MMS1 (Figure 5) not only inside SLAMS 2 but also between SLAMS 3 and SLAMS 2. The magnetic reconnection may contribute to the destruction of the SLAMSs. Magnetic reconnection is characterized by high-speed electron flow ($|V_L| > 100$ km/s, $|V_M| > 300$ km/s, $V_{Alfvén}$ = 36.35 km/s) and an intense reconnection electric field along the M direction, hall electric field along the N direction, and energy conversion at the current sheet (Figure 5). There is no significant electron heating (Figure 5b) and ion jet while crossing the current sheet (Figure 5d), and the current sheet thickness is below the ion inertia length (green bars in Figure 5c). These observational features are consistent with the electron-only reconnection process, while ions do not participate in these magnetic reconnection processes [53,54]. However, as magnetic field topology changes during reconnection, local conditions are no longer suitable for the nonlinear evolution of the ion-ion non-resonant mode, resulting in a reduction in the free energy of harmonic sidebands. In addition, the stored energy in the magnetic field is dissipated during reconnection, which may also hasten the destruction of SLAMS 2 and SLAMS 3 observed by the MMS.
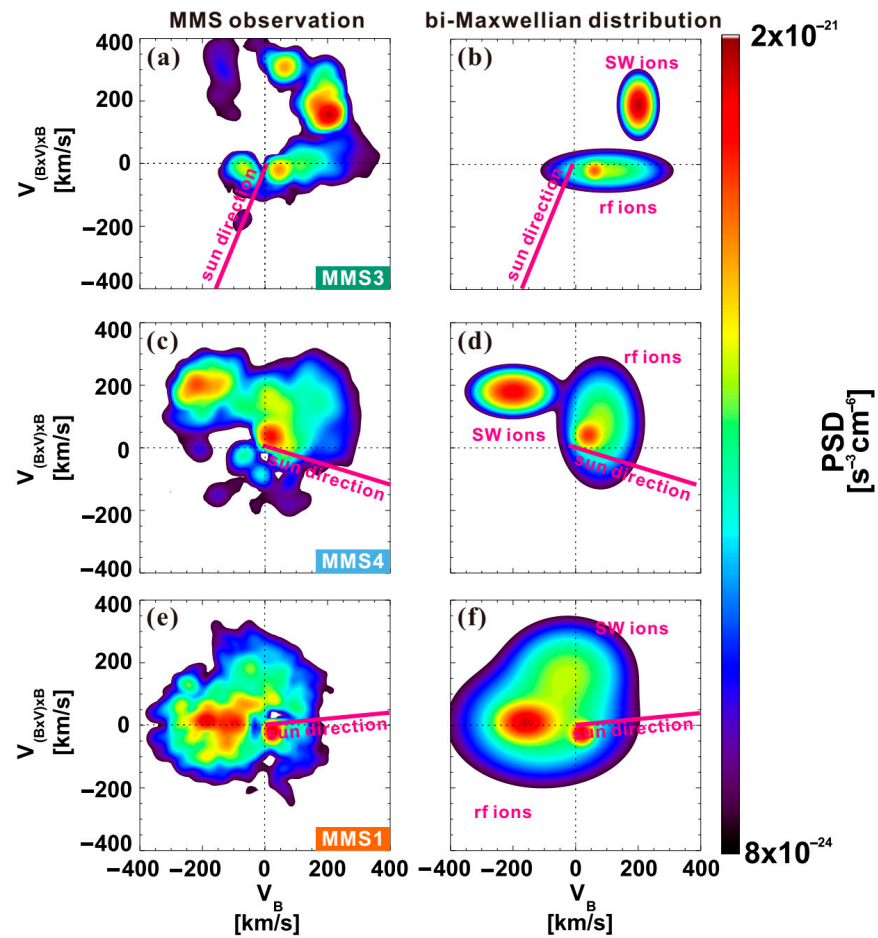
Figure 3. The ion distribution (in unit of s-3 cm-6) in the plane parallel to the magnetic field during the time interval of SLAMS3 observed by (**a**) MMS3, (**c**) MMS 4, and (**e**) MMS1 and the corresponding bi-Maxwellian fitting in (**b**,**d**,**f**). The solar wind ions and reflected ions are marked by magenta text in (**b**,**d**,**f**). The sun direction is marked by the magenta lines.

Table 1. Drift bi-Maxwellian fitting parameters and the saturation amplitude of the ion-ion non-resonate mode.

| Satellite	Ion	Density $(1/cm^{-3})$	$V_{th\parallel}$ (km/s)	$V_{th\perp}$ (km/s)	$V_{drift\parallel}$ (km/s)	$V_{drift\perp}$ (km/s)	$\delta B/B_0$ from MMS	$\delta B/B_0$
MMS 3	Solar wind ions (SW)	0.7	30	50	200	190	/	0.93
	Reflected ions (rf)	0.2	120	40	100	−20		
	Background ions	0.02	20	20	20	−20		
MMS 4	Solar wind ions	0.7	70	40	−200	180	1.79	1.84
	Reflected ions	1.2	80	120	80	80		
	Background ions	0.1	30	30	40	0		
MMS 1	Solar wind ions	0.7	60	40	−160	10	2.81	3.21
	Reflected ions	1.2	125	100	−25	175		
	Background ions	0.12	25	25	20	−25		
		2.5	175	120	−105	10		
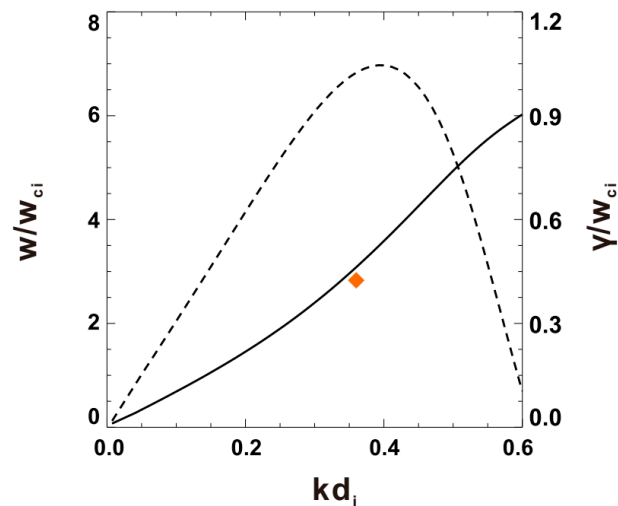
Figure 4. Dispersion relation using model parameters by fitting the ion distribution of MMS3. Real frequency (solid curve) and growth rate (dashed curve) of the ion-ion non-resonant mode. The orange in diamond marks the real frequency and the wave number for MMS observations.
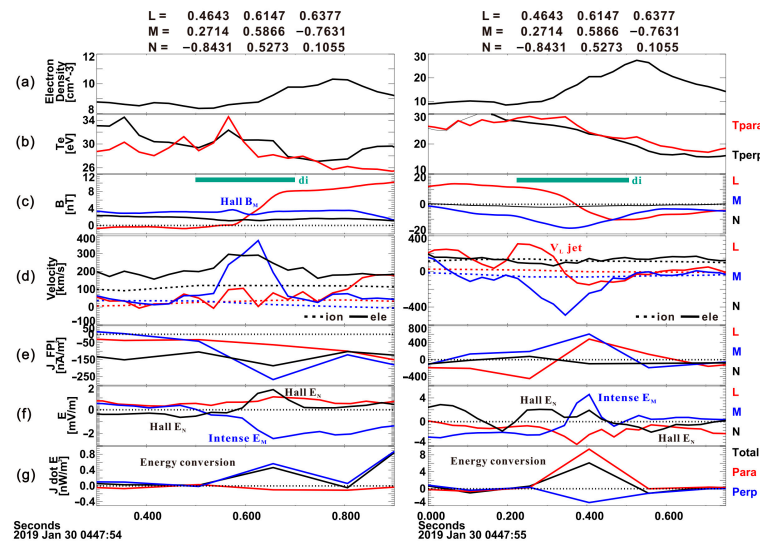

Figure 5. MMS1 observation of current sheets in the LMN coordinate system between SLAMS 3 and SLAMS 2 (left panels)/inside SLAMS 2 (right panels): (**a**) electron density, (**b**) electron temperature, red/blue curves for parallel/perpendicular temperature (**c**) magnetic field, (**d**) electron (solid curve) and ion (dashed curve) velocity, (**e**) current density obtained from the FPI observation, (**f**) electric field, and (**g**) the energy dissipation of perpendicular (blue curves) and parallel components (red curves) and the sum of J·E′. L/M/N components are represented by red/blue/black curves. The detailed information of L-M-N coordinates in GSM coordinates are shown on the top of this figure. The ion inertial length is indicated by green bars in (**c**).

4. Conclusions

Based on MMS constellation observations, we observed the entire rise and fall of SLAMSs for the first time. The wave properties and instability analysis indicate SLAMSs steepening, driven by the ion-ion right-hand non-resonant mode. Non-linearly generated harmonic sidebands locally superimpose, while the thermalized solar wind and reflected ions provide free energy for the enhancement of the magnetic field.

As the steepening progresses, the gradient length of SLAMSs shortens [55], demagnetizing ions while electrons remain magnetized. This triggers the modified two-stream instability [56–59], generating waves near the lower-hybrid frequency (Figure 2e,g). Subsequently, dissipation and dispersion occur, which limit or balance the nonlinear process and

prevent the destruction of SLAMSs. However, with an increase in the anti-parallel compo-
nent of the magnetic field and a decrease in the thickness of the current sheet generated
inside the SLAMS, magnetic reconnection occurs during steepening [25]. This alters the
field line topology, introducing dissipation contributing to the destruction of SLAMS 3 and
SLAMS 2, as recorded by MMS1 and MMS2.

In summary, this study investigates the rise and fall of SLAMSs, which reflects the
formation and dissipation processes of shock waves to some extent and sheds new light on
the energy conversion near the shock and shock evolution across the universe. However,
the SLAMS evolution in this case is under a high Alfvén Mach number solar wind condition
(MA = 14.8). Statistical analysis is required to determine whether the evolution process of
SLAMSs varies under various solar wind conditions.

References

1. Burgess, D.; Lucek, E.A.; Scholer, M.; Bale, S.D.; Balikhin, M.A.; Balogh, A.; Horbury, T.S.; Krasnoselskikh, V.V.; Kucharek, H.; Lembège, B.; et al. Quasi-parallel shock structure and processes. *Space Sci. Rev.* **2005**, *118*, 205–222. [CrossRef]
2. Bale, S.D.; Balikhin, M.A.; Horbury, T.S.; Krasnoselskikh, V.V.; Kucharek, H.; Möbius, E.; Walker, S.N.; Balogh, A.; Burgess, D.; Lembège, B.; et al. Quasi-perpendicular shock structure and processes. *Space Sci. Rev.* **2005**, *118*, 161–203. [CrossRef]
3. Zhang, H.; Zong, Q.G.; Connor, H.; Delamere, P.; Facskó, G.; Han, D.S.; Hasegawa, H.; Kallio, E.; Kis, A.; Le, G.; et al. Dayside Transient Phenomena and Their Impact on the Magnetosphere and Ionosphere. *Space Sci. Rev.* **2022**, *218*, 40. [CrossRef] [PubMed]
4. Gary, S.P. Electromagnetic Ion Ion Instabilities and Their Consequences in Space Plasmas—A Review. *Space Sci. Rev.* **1991**, *56*, 373–415. [CrossRef]
5. Hada, T.; Kennel, C.F.; Terasawa, T. Excitation of Compressional Waves and the Formation of Shocklets in the Earth's Foreshock. *J. Geophys. Res. Space Phys.* **1987**, *92*, 4423–4435. [CrossRef]
6. Omidi, N.; Winske, D. Steepening of Kinetic Magnetosonic Waves into Shocklets—Simulations and Consequences for Planetary Shocks and Comets. *J. Geophys. Res. Space Phys.* **1990**, *95*, 2281–2300. [CrossRef]
7. Dubouloz, N.; Scholer, M. 2-Dimensional Simulations of Magnetic Pulsations Upstream of the Earth's Bow Shock. *J. Geophys. Res. Space Phys.* **1995**, *100*, 9461–9474. [CrossRef]
8. Onsager, T.G.; Winske, D.; Thomsen, M.F. Interaction of a Finite-Length Ion-Beam with a Background Plasma—Reflected Ions at the Quasi-Parallel Bow Shock. *J. Geophys. Res. Space Phys.* **1991**, *96*, 1775–1788. [CrossRef]
9. Hoppe, M.M.; Russell, C.T.; Frank, L.A.; Eastman, T.E.; Greenstadt, E.W. Upstream Hydromagnetic-Waves and Their Association with Backstreaming Ion Populations—Isee-1 and Isee-2 Observations. *J. Geophys. Res. Space Phys.* **1981**, *86*, 4471–4492. [CrossRef]
10. Lucek, E.A.; Horbury, T.S.; Balogh, A.; Dandouras, I.; Rème, H. Cluster observations of structures at quasi-parallel bow shocks. *Ann. Geophys.* **2004**, *22*, 2309–2313. [CrossRef]
11. Lucek, E.A.; Horbury, T.S.; Dandouras, I.; Rème, H. Cluster observations of the Earth's quasi-parallel bow shock. *J. Geophys. Res. Space Phys.* **2008**, *113*. [CrossRef]
12. Mann, G.; Luhr, H.; Baumjohann, W. Statistical-Analysis of Short Large-Amplitude Magnetic-Field Structures in the Vicinity of the Quasi-Parallel Bow Shock. *J. Geophys. Res. Space Phys.* **1994**, *99*, 13315–13323. [CrossRef]
13. Schwartz, S.J.; Burgess, D. Quasi-Parallel Shocks—A Patchwork of 3-Dimensional Structures. *Geophys. Res. Lett.* **1991**, *18*, 373–376. [CrossRef]

14. Wilson, L.B. Low Frequency Waves at and Upstream of Collisionless Shocks. In *Low-Frequency Waves in Space Plasmas*; John Wiley & Sons: Hoboken, NJ, USA, 2016; pp. 269–291.

15. Wilson, L.B.; Koval, A.; Sibeck, D.G.; Szabo, A.; Cattell, C.A.; Kasper, J.C.; Maruca, B.A.; Pulupa, M.; Salem, C.S.; Wilber, M. Shocklets, SLAMS, and field-aligned ion beams in the terrestrial foreshock. *J. Geophys.Res. Space Phys.* **2013**, *118*, 957–966. [CrossRef]

16. Bai, S.C.; Shi, Q.Q.; Zhang, H.; Guo, R.L.; Shen, X.C.; Liu, T.Z.; Degeling, A.W.; Tian, A.M.; Bu, Y.D.; Zhang, S.; et al. Electron Dynamics and Whistler-Mode Waves Inside the Short Large-Amplitude Magnetic Field Structures. *J. Geophys. Res. Space Phys.* **2023**, *128*, e2023JA031816. [CrossRef]

17. Bai, S.-C.; Shi, Q.; Shen, X.-C.; Tian, A.; Zhang, H.; Guo, R.; Wang, M.; Degeling, A.W.; Bu, Y.; Zhang, S.; et al. Whistler-Mode Waves Inside Short Large-Amplitude Magnetic Field Structures: Characteristics and Generation Mechanisms. *J. Geophys. Res. Space Phys.* **2024**, *129*, e2023JA032392. [CrossRef]

18. Liu, T.Z.; Hao, Y.F.; Wilson, L.B.; Turner, D.L.; Zhang, H. Magnetospheric Multiscale Observations of Earth's Oblique Bow Shock Reformation by Foreshock Ultralow-Frequency Waves. *Geophys. Res. Lett.* **2021**, *48*, e2020GL091184. [CrossRef]

19. Johlander, A.; Battarbee, M.; Turc, L.; Ganse, U.; Pfau-Kempf, Y.; Grandin, M.; Suni, J.; Tarvus, V.; Bussov, M.; Zhou, H.Y.; et al. Quasi-Parallel Shock Reformation Seen by Magnetospheric Multiscale and Ion-Kinetic Simulations. *Geophys. Res. Lett.* **2022**, *49*, e2021GL096335. [CrossRef]

20. Bessho, N.; Chen, L.J.; Wang, S.; Hesse, M.; Wilson, L.B. Magnetic Reconnection in a Quasi-Parallel Shock: Two-Dimensional Local Particle-in-Cell Simulation. *Geophys. Res. Lett.* **2019**, *46*, 9352–9361. [CrossRef]

21. Bessho, N.; Chen, L.J.; Wang, S.; Hesse, M.; Wilson, L.B.; Ng, J. Magnetic reconnection and kinetic waves generated in the Earth's quasi-parallel bow shock. *Phys. Plasmas* **2020**, *27*, 092901. [CrossRef]

22. Gingell, I.; Schwartz, S.J.; Burgess, D.; Johlander, A.; Russell, C.T.; Burch, J.L.; Ergun, R.E.; Fuselier, S.; Gershman, D.J.; Giles, B.L.; et al. MMS Observations and Hybrid Simulations of Surface Ripples at a Marginally Quasi-Parallel Shock. *J. Geophys. Res. Space Phys.* **2017**, *122*, 11003–11017. [CrossRef]

23. Gingell, I.; Schwartz, S.J.; Eastwood, J.P.; Burch, J.L.; Ergun, R.E.; Fuselier, S.; Gershman, D.J.; Giles, B.L.; Khotyaintsev, Y.V.; Lavraud, B.; et al. Observations of Magnetic Reconnection in the Transition Region of Quasi-Parallel Shocks. *Geophys. Res. Lett.* **2019**, *46*, 1177–1184. [CrossRef]

24. Wang, S.; Chen, L.J.; Bessho, N.; Hesse, M.; Wilson, L.B.; Giles, B.; Moore, T.E.; Russell, C.T.; Torbert, R.B.; Burch, J.L. Observational Evidence of Magnetic Reconnection in the Terrestrial Bow Shock Transition Region. *Geophys. Res. Lett.* **2019**, *46*, 562–570. [CrossRef]

25. Wang, S.; Chen, L.J.; Bessho, N.; Hesse, M.; Wilson, L.B.; Denton, R.; Ng, J.; Giles, B.; Torbert, R.; Burch, J. Ion-scale Current Structures in Short Large-amplitude Magnetic Structures. *Astrophys. J.* **2020**, *898*, 121. [CrossRef]

26. Bai, S.C.; Shi, Q.Q.; Liu, T.Z.; Zhang, H.; Yue, C.; Sun, W.J.; Tian, A.M.; Degeling, A.W.; Bortnik, J.; Rae, I.J.; et al. Ion-Scale Flux Rope Observed inside a Hot Flow Anomaly. *Geophys. Res. Lett.* **2020**, *47*, e2019GL085933. [CrossRef]

27. Liu, T.Z.; Lu, S.; Turner, D.L.; Gingell, I.; Angelopoulos, V.; Zhang, H.; Artemyev, A.; Burch, J.L. Magnetospheric Multiscale (MMS) Observations of Magnetic Reconnection in Foreshock Transients. *J. Geophys. Res. Space Phys.* **2020**, *125*, e2020JA027822. [CrossRef]

28. Treumann, R.A. Fundamentals of collisionless shocks for astrophysical application, 1. Non-relativistic shocks. *Astron. Astrophys. Rev.* **2009**, *17*, 409–535. [CrossRef]

29. Raptis, S.; Karlsson, T.; Plaschke, F.; Kullen, A.; Lindqvist, P.A. Classifying Magnetosheath Jets Using MMS: Statistical Properties. *J. Geophys. Res. Space Phys.* **2020**, *125*, e2019JA027754. [CrossRef]

30. Karlsson, T.; Kullen, A.; Liljeblad, E.; Brenning, N.; Nilsson, H.; Gunell, H.; Hamrin, M. On the origin of magnetosheath plasmoids and their relation to magnetosheath jets. *J. Geophys. Res. Space Phys.* **2015**, *120*, 7390–7403. [CrossRef]

31. Plaschke, F.; Hietala, H.; Archer, M.; Blanco-Cano, X.; Kajdic, P.; Karlsson, T.; Lee, S.H.; Omidi, N.; Palmroth, M.; Roytershteyn, V.; et al. Jets Downstream of Collisionless Shocks. *Space Sci. Rev.* **2018**, *214*, 81. [CrossRef]

32. Wang, X.Y.; Lin, Y. Generation of nonlinear Alfven and magnetosonic waves by beam-plasma interaction. *Phys. Plasmas* **2003**, *10*, 3528–3538. [CrossRef]

33. Winske, D.; Leroy, M.M. Diffuse Ions Produced by Electromagnetic Ion-Beam Instabilities. *J. Geophys. Res. Space Phys.* **1984**, *89*, 2673–2688. [CrossRef]

34. Akimoto, K.; Winske, D.; Gary, S.P.; Thomsen, M.F. Nonlinear Evolution of Electromagnetic Ion-Beam Instabilities. *J. Geophys. Res. Space Phys.* **1993**, *98*, 1419–1433. [CrossRef]

35. Gary, S.P.; Smith, C.W.; Lee, M.A.; Goldstein, M.L.; Forslund, D.W. Electromagnetic Ion-Beam Instabilities. *Phys. Fluids* **1984**, *27*, 1852–1862. [CrossRef]

36. Le, G.; Russell, C.T. The Morphology of ULF Waves in the Earth's Foreshock. In *Solar Wind Sources of Magnetospheric Ultra-Low-Frequency Waves*; John Wiley & Sons: Hoboken, NJ, USA, 1994; pp. 87–98.

37. Scholer, M. Upstream waves, shocklets, short large-amplitude magnetic structures and the cyclic behavior of oblique quasi-parallel collisionless shocks. *J. Geophys. Res. Space Phys.* **1993**, *98*, 47–57. [CrossRef]

38. Giacalone, J.; Schwartz, S.J.; Burgess, D. Observations of suprathermal ions in association with SLAMS. *Geophys. Res. Lett.* **1993**, *20*, 149–152. [CrossRef]

39. Schwartz, S.J.; Burgess, D.; Wilkinson, W.P.; Kessel, R.L.; Dunlop, M.; Luhr, H. Observations of Short Large-Amplitude Magnetic-Structures at a Quasi-Parallel Shock. *J. Geophys. Res. Space Phys.* **1992**, *97*, 4209–4227. [CrossRef]

40. Scholer, M.; Kucharek, H.; Shinohara, I. Short large-amplitude magnetic structures and whistler wave precursors in a full-particle quasi-parallel shock simulation. *J. Geophys. Res. Space Phys.* **2003**, *108*. [CrossRef]

41. Tsubouchi, K.; Lembège, B. Full particle simulations of short large-amplitude magnetic structures (SLAMS) in quasi-parallel shocks. *J. Geophys. Res. Space Phys.* **2004**, *109*. [CrossRef]

42. Chen, L.J.; Wang, S.; Ng, J.; Bessho, N.; Tang, J.M.; Fung, S.F.; Le, G.; Gershman, D.; Giles, B.; Russell, C.T.; et al. Solitary Magnetic Structures at Quasi-Parallel Collisionless Shocks: Formation. *Geophys. Res. Lett.* **2021**, *48*, e2020GL090800. [CrossRef]

43. Burch, J.L.; Moore, T.E.; Torbert, R.B.; Giles, B.L. Magnetospheric Multiscale Overview and Science Objectives. *Space Sci. Rev.* **2016**, *199*, 5–21. [CrossRef]

44. Russell, C.T.; Anderson, B.J.; Baumjohann, W.; Bromund, K.R.; Dearborn, D.; Fischer, D.; Le, G.; Leinweber, H.K.; Leneman, D.; Magnes, W.; et al. The Magnetospheric Multiscale Magnetometers. *Space Sci. Rev.* **2016**, *199*, 189–256. [CrossRef]

45. Pollock, C.; Moore, T.; Jacques, A.; Burch, J.; Gliese, U.; Saito, Y.; Omoto, T.; Avanov, L.; Barrie, A.; Coffey, V.; et al. Fast Plasma Investigation for Magnetospheric Multiscale. *Space Sci. Rev.* **2016**, *199*, 331–406. [CrossRef]

46. Lindqvist, P.A.; Olsson, G.; Torbert, R.B.; King, B.; Granoff, M.; Rau, D.; Needell, G.; Turco, S.; Dors, I.; Beckman, P.; et al. The Spin-Plane Double Probe Electric Field Instrument for MMS. *Space Sci. Rev.* **2016**, *199*, 137–165. [CrossRef]

47. Ergun, R.E.; Tucker, S.; Westfall, J.; Goodrich, K.A.; Malaspina, D.M.; Summers, D.; Wallace, J.; Karlsson, M.; Mack, J.; Brennan, N.; et al. The Axial Double Probe and Fields Signal Processing for the MMS Mission. *Space Sci. Rev.* **2016**, *199*, 167–188. [CrossRef]

48. Chao, J.K.; Wu, D.J.; Lin, C.H.; Yang, Y.H.; Wang, X.; Kesse, M.; Chen, S.H.; Lepping, R.P. Models for the size and shape of the Earth's magnetopause and bow shock. *Cospar Colloq.* **2002**, *12*, 127–135.

49. Sonnerup, B.U.Ö. Magnetic field reconnection. In *Solar System Plasma Physics*; Lanzerotti, L.J., Kennel, C.F., Parker, E.N., Eds.; North Holland: Amsterdam, The Netherlands, 1979; Volume 3.

50. Sonnerup, B.U.Ö.; Scheible, M. Minimum and maximum variance analysis, in Analysis Methods for Multi-Spacecraft Data. In *Analysis Methods for Multi-Spacecraft Data*; Paschmann, G., Daly, P.W., Eds.; ESA Publications Division: Noordwijk, The Netherlands, 1998; pp. 185–220.

51. Zahibo, N.; Slunyaev, A.; Talipova, T.; Pelinovsky, E.; Kurkin, A.; Polukhina, O. Strongly nonlinear steepening of long interfacial waves. *Nonlinear Proc. Geophys.* **2007**, *14*, 247–256. [CrossRef]

52. Xie, H.S. BO: A unified tool for plasma waves and instabilities analysis. *Comput. Phys. Commun.* **2019**, *244*, 343–371. [CrossRef]

53. Phan, T.D.; Eastwood, J.P.; Shay, M.A.; Drake, J.F.; Sonnerup, B.U.Ö.; Fujimoto, M.; Cassak, P.A.; Oieroset, M.; Burch, J.L.; Torbert, R.B.; et al. Electron magnetic reconnection without ion coupling in Earth's turbulent magnetosheath. *Nature* **2018**, *557*, 202–206. [CrossRef]

54. Lu, S.; Lu, Q.M.; Wang, R.S.; Pritchett, P.L.; Hubbert, M.; Qi, Y.; Huang, K.; Li, X.M.; Russell, C.T. Electron-Only Reconnection as a Transition From Quiet Current Sheet to Standard Reconnection in Earth's Magnetotail: Particle-In-Cell Simulation and Application to MMS Data. *Geophys. Res. Lett.* **2022**, *49*, e2022GL098547. [CrossRef]

55. Kennel, C.F.; Edmiston, J.P.; Hada, T. A Quarter Century of Collisionless Shock Research. In *Collisionless Shocks in the Heliosphere: A Tutorial Review*; American Geophysical Union: Washington, DC, USA, 1985; pp. 1–36.

56. Muschietti, L.; Lembège, B. Two-stream instabilities from the lower-hybrid frequency to the electron cyclotron frequency: Application to the front of quasi-perpendicular shocks. *Ann. Geophys.* **2017**, *35*, 1093–1112. [CrossRef]

57. Wu, C.S.; Zhou, Y.M.; Tsai, S.T.; Guo, S.C.; Winske, D.; Papadopoulos, K. A Kinetic Cross-Field Streaming Instability. *Phys. Fluids* **1983**, *26*, 1259–1267. [CrossRef]

58. Mcbride, J.B.; Ott, E.; Boris, J.P.; Orens, J.H. Theory and Simulation of Turbulent Heating by Modified 2-Stream Instability. *Phys. Fluids* **1972**, *15*, 2367–2383. [CrossRef]

59. Lemons, D.S.; Winske, D.; Gary, S.P. Non-Linear Theory and Computer-Simulation of Weibel Instability. *Bull. Am. Phys. Soc.* **1978**, *23*, 607.

60. Angelopoulos, V.; Cruce, P.; Drozdov, A.; Grimes, E.W.; Hatzigeorgiu, N.; King, D.A.; Larson, D.; Lewis, J.W.; McTiernan, J.M.; Roberts, D.A.; et al. The Space Physics Environment Data Analysis System (SPEDAS). *Space Sci. Rev.* **2019**, *215*, 9. [CrossRef]